ACS OMEGA

http://pubs.acs.org/journal/acsodf

Article

In Situ-Grown Heterostructured Co_3S_4/CNTs/C Nanocomposites with a Bridged Structure for High-Performance Supercapacitors

Yuqing Qiao,* Fan Wang, Na Li, Weimin Gao, and Tifeng Jiao*

Cite This: *ACS Omega* 2021, 6, 33855−33863

Read Online

ACCESS | Metrics & More | Article Recommendations

ABSTRACT: As one of the most competitive candidates for energy storage devices, supercapacitors have attracted extensive research interest due to their incomparable power density and ultralong cycling stability. However, the large surface area required for charge storage is an irreconcilable contradiction with the requirement of energy density. Therefore, a high energy density is a major challenge for supercapacitors. To solve the contradiction, Co_3S_4/CNTs/C with a bridged structure is designed, where CNTs generated in situ serve as a bridge to connect a porous carbon matrix and a Co_3S_4 nanoparticle, and Co_3S_4 nanoparticles are anchored on the topmost of CNTs. The porous carbon and Co_3S_4 are used for electrochemical double-layer capacitors and pseudocapacitors, respectively. This bridged structure can efficiently utilize the surface of Co_3S_4 nanoparticles to increase the overall energy storage capacity and provide more electrochemically active sites for charge storage and delivery. The materials show an energy density of 41.3 Wh kg^{-1} at 691.9 W kg^{-1} power density and a retaining energy density of 33.1 Wh kg^{-1} at a high power density of 3199.9 W kg^{-1} in an asymmetrical supercapacitor. The synthetic technique provides a simple method to obtain heterostructured nanocomposites with a high energy density by maximizing the effect of pseudocapacitor electrode active materials.

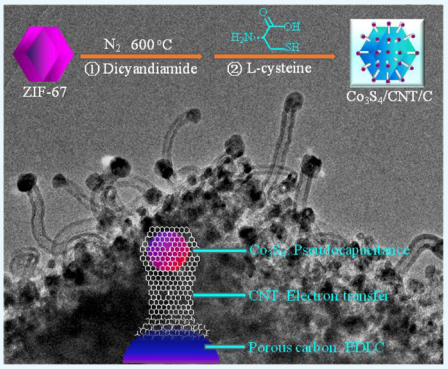

1. INTRODUCTION

Supercapacitors, as energy storage devices, exhibit incomparable power density and ultralong cycling stability than secondary batteries.[1−7] However, its energy density is unsatisfactory. Based on the charge storage mechanism, supercapacitors can be divided into electrochemical double-layer capacitors and pseudocapacitors. Electrochemical double-layer capacitors (EDLCs) are generally characterized by a rapid charge−discharge process, high-power density, and long-life cycle. EDLCs employ carbon-based materials, such as porous carbon, as active electrode materials. Charge storage mainly depends on the electrochemical adsorption/desorption of ions at the electrode/electrolyte interface. The energy density and energy storage capacity of those supercapacitors are limited by the specific surface area.[8−12] Pseudocapacitors are based on the rapid surface faradic redox reactions to store electric energy. They can provide much great energy storage capacity than EDLCs, as the materials used in the type of supercapacitor, such as transition metal oxides, could perform at a specific capacitance close to their theoretical value.[13−15] However, their power density and life cycle are lower due to the chemical reactions involved in the charge−discharge process and low electrical conductivity. Therefore, many efforts have been made to increase the energy density by combining the advantages of EDLCs and pseudocapacitors.[16−18]

The energy density of a supercapacitor depends on its capacitance and the working voltage, following $E = 0.5CU^2$, where E is the energy density (Wh kg^{-1}), C is the specific capacitance (F g^{-1}), and U is the overall voltage (V). One approach to increase energy density is to develop electrode active materials with a large specific capacitance.[1−3] Based on the charge surface-storage mechanism, a porous structure in nanoscale is indispensable for electrode materials that could combine EDLC and pseudocapacitor features, which have exhibited its potential in this regard.[15−17] The emergence of new structures such as embedded and wrapped structures provides new concepts for the combination of EDLC and pseudocapacitor electrodes to improve energy density.[18−21] Among numerous supercapacitor electrode materials, Co_3S_4 is regarded as a promising electrode material for commercial supercapacitors due to its environmental-friendly feature and low cost.[20] The performance of Co_3S_4 depends on its structure, morphology, and components, such as nanostructure, porous structure, or composite with other materials, and it is critical for Co_3S_4 with encouraging electrochemical performances such as high rate capability and long cycle life.[21]

Received: September 16, 2021
Accepted: November 23, 2021
Published: December 3, 2021

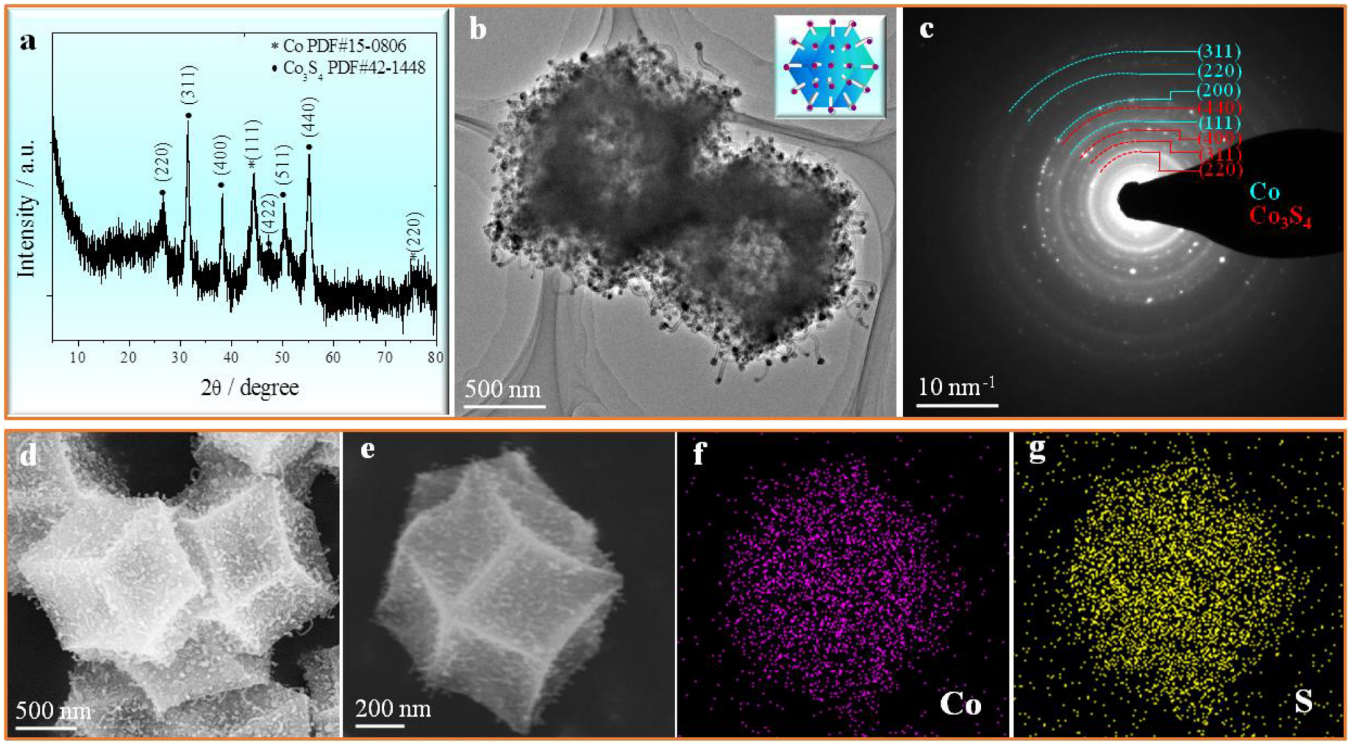

Figure 1. Structure characteristics of the Co_3S_4/CNTs/C nanocomposites derived from ZIF-67. (a) XRD of the nanocomposites; (b, c) TEM and EDP of the nanocomposites; (d, e) SEM images and (f, g) EDS mappings of the nanocomposites.

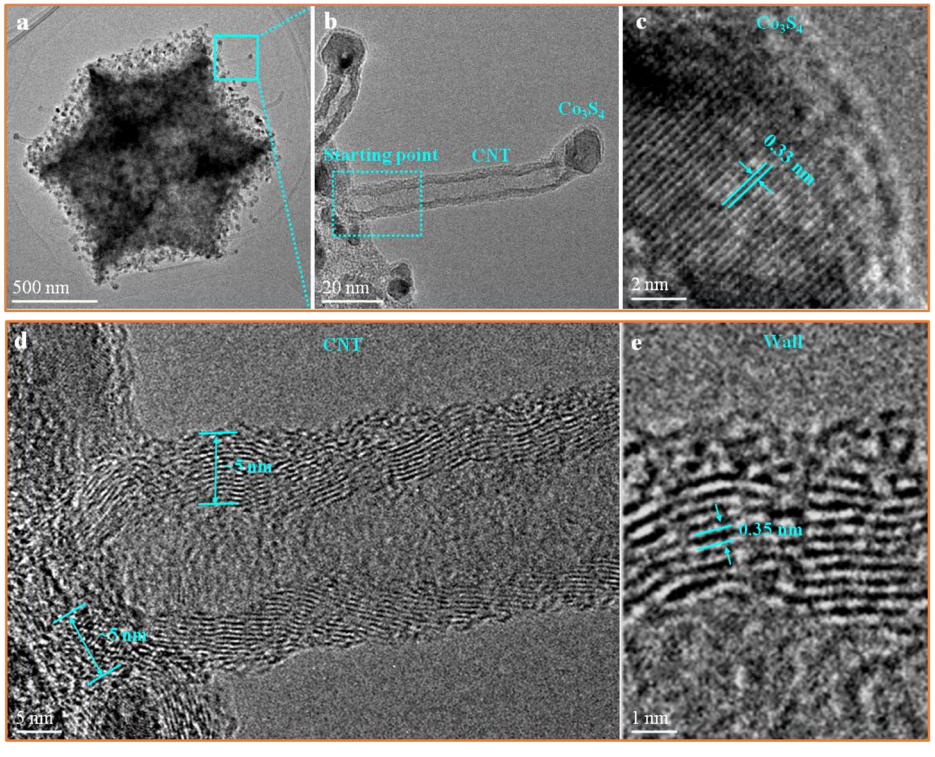

Figure 2. (a) TEM image of Co_3S_4/CNTs/C nanocomposites, (b) morphology of a CNT with a Co_3S_4 nanoparticle anchored on its end, and (c–e) high-resolution images of a Co_3S_4 nanoparticle with a crystal structure, the starting point, and the wall (about 10 layers, $d \approx 0.35$ nm) of the CNT.

As a typical family of novel materials, metal–organic frameworks (MOFs) are porous materials with a high specific surface area, large pore volumes, and tunable pore size. MOFs and MOF-derived materials (porous carbon materials and nanostructured metal or metal oxide materials) have demonstrated promising performances in the field of energy storage and conversion, such as Li-based batteries, Na-ion batteries, fuel cells, solar cells, and supercapacitors.[22] In the

https://doi.org/10.1021/acsomega.1c05081
ACS Omega 2021, 6, 33855−33863

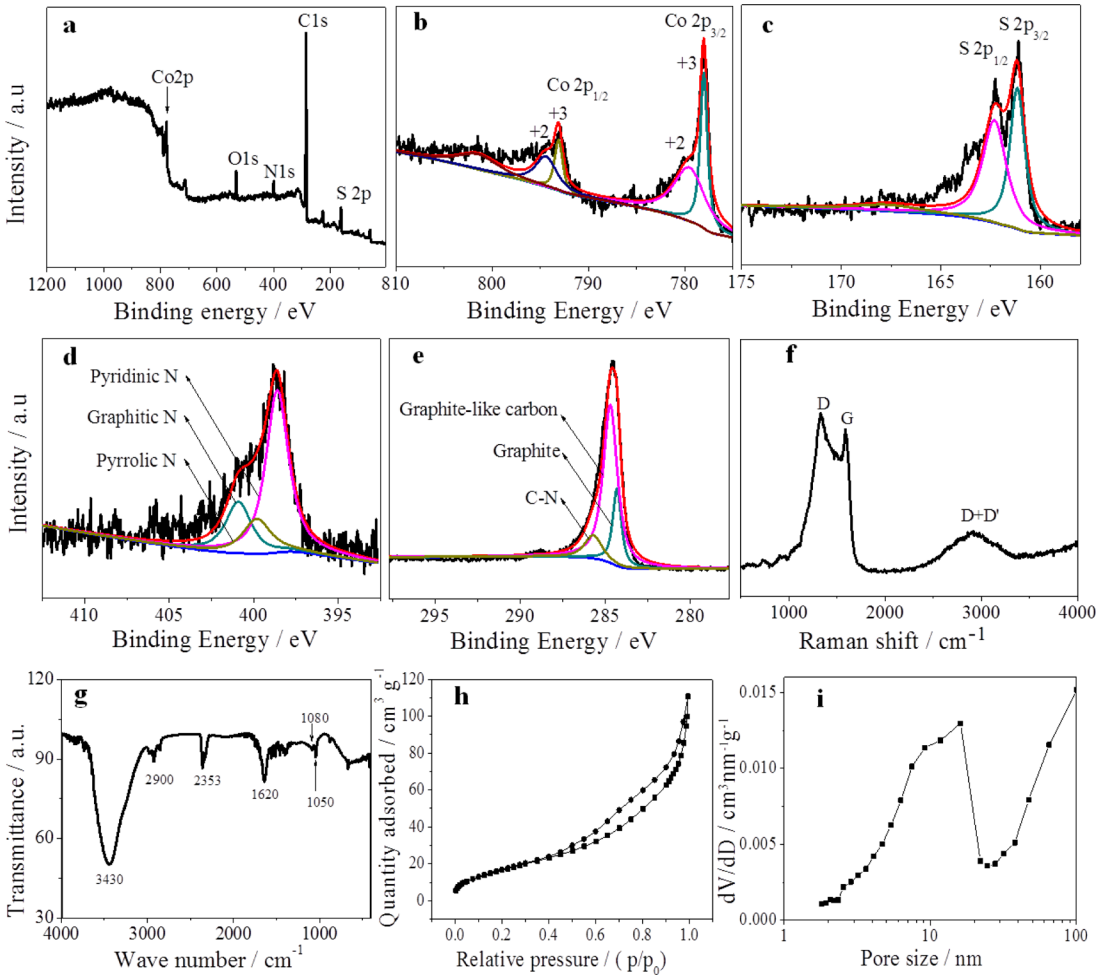

Figure 3. (a–e) XPS spectra of the Co 2p level, S 2p level, and N 1s level on Co_3S_4/CNTs/C nanocomposites; (f) Raman, (g) FT-IR, (h) nitrogen adsorption–desorption isotherms, and (i) porosity of the MOF-derived Co_3S_4/CNTs/C nanocomposites.

present work, Co_3S_4/CNTs/C nanocomposites with a bridged structure are constructed through the in situ growth of MOF-derived Co/C nanoparticles. ZIF-67 was carbonized to form Co nanoparticles in a porous carbon matrix first, and then it acts as a catalyst to prepare in situ CNTs synchronously. With the growth of CNTs, Co nanoparticles located on the endmost of CNTs are shifted from the inside to the outside; as a result, the location of Co nanoparticles is re-adjusted, which is convenient for the following sulfuration with L-cysteine used as a vulcanizing agent. In the nanocomposites, CNTs act as the bridges, Co_3S_4 nanoparticles located at the endmost of the bridges act as pseudocapacitors, and porous carbons are used for EDLCs.

2. RESULTS AND DISCUSSION

2.1. Structure Characterization. The Co_3S_4 phase is observed from the X-ray diffraction (XRD) patterns of Co_3S_4/CNTs/C nanocomposites (Figure 1a), according to the standard card PDF42-1448 (cubic structure; space group: *Fd*-3*m* (22); a = 9.437 Å; vol = 840.4 Å^3). The peaks at 31.4°, 37.9°, and 55.2° correspond to the (311), (400), and (440) planes, respectively. The particle sizes calculated from the half-width of those diffraction peaks are 11.1, 12.2, and 11.6 nm, respectively. The morphology and phase constitution of the Co_3S_4/CNTs/C nanocomposites were revealed by transmission electron microscopy (TEM) and the electron diffraction pattern (EDP) (Figure 1b,c). The Co_3S_4/CNTs/C nanocomposites indicated a bridged structure. Those CNTs indicated monodispersed characterization without entangling. In addition, the Co_3S_4/CNTs/C nanocomposites have a rhombic dodecahedron shape, which is inherent from the ZIF-67 precursor (Figure 1b,d). The scanning electron microscopy (SEM) image and corresponding EDS mapping of the Co_3S_4/CNTs/C nanocomposites are shown in Figure 1e–g, indicating the even distribution of Co and S elements.

The TEM image and high-resolution images of the CNT and Co_3S_4 in the Co_3S_4/CNTs/C nanocomposites are shown in Figure 2. The monodispersed CNTs have a length of about 100 nm with a diameter of about 15 nm (Figure 2b). Figure 2c shows the high-resolution image of a Co_3S_4 nanoparticle anchored on the endmost of the CNTs. Figure 2d shows a sealed multiwalled CNT with an inner diameter of about 5 nm and a thickness of about 5 nm. Figure 2d also shows that the CNT wall is composed of graphite carbon with a high defect density and a multilayer structure with an interlamellar spacing of 0.35 nm (Figure 2e). The nanoscale size and monodispersed characteristic of the Co_3S_4 particles explicitly revealed that they have a large specific surface area, which would be convenient for the permeation of the electrolyte during the process of charge storage/delivery and result in a high specific capacitance. The monodispersed nanosized Co_3S_4 particles may present a typical capacitance behavior with a linear

https://doi.org/10.1021/acsomega.1c05081
ACS Omega 2021, 6, 33855–33863

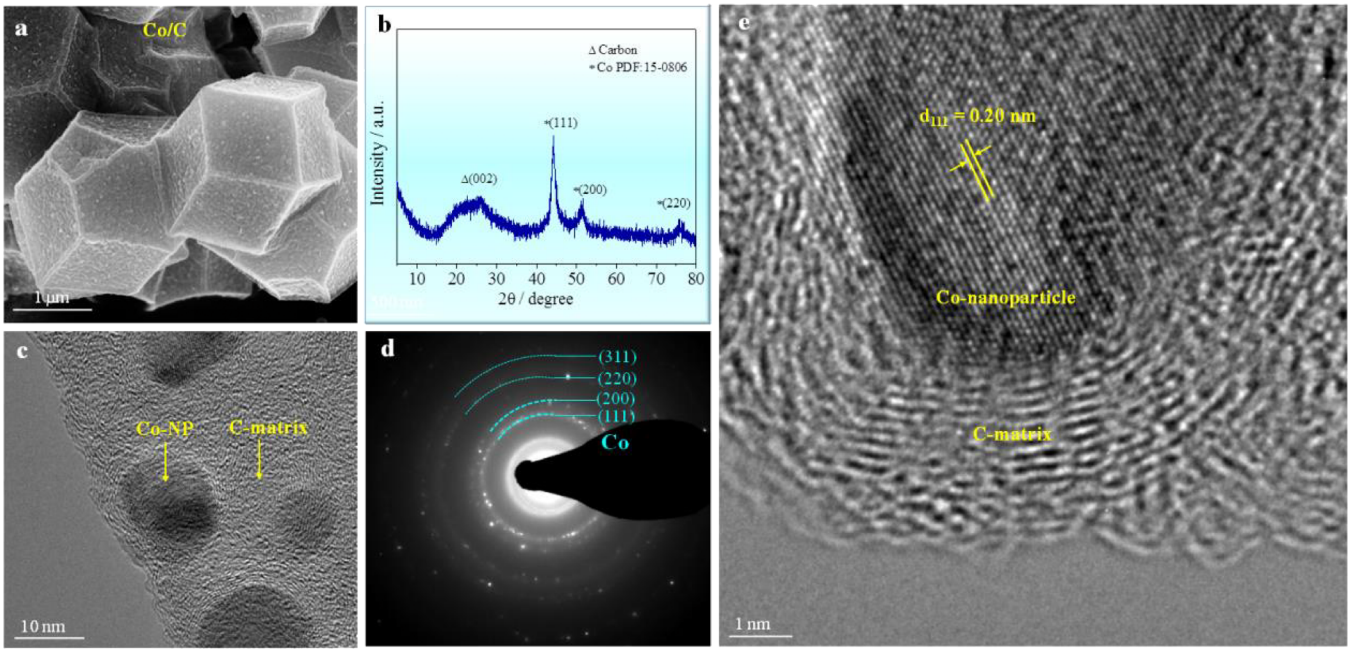

Figure 4. Structure characteristics of Co/C nanocomposites derived from ZIF-67. (a) Morphology of the Co/C nanocomposites with a rhombic dodecahedron shape; (b) XRD; (c) high-resolution image of the Co/C nanocomposites with monodispersed Co nanoparticles dispersed in a porous carbon matrix; (d) EDP of the Co/C nanocomposites; (e) amplified high-resolution image of a Co/C nanoparticle, showing the Co nanoparticle with a monocrystal structure and the carbon matrix with a lamellar graphene structure.

dependence of the charge stored on the width of the potential window.

The elemental state of the as-synthesized Co_3S_4/CNTs/C nanocomposites was confirmed by X-ray photoelectron spectroscopy (XPS) (Figure 3a–e). For cobalt (Co) 2p shown in the high-resolution spectrum (Figure 3b), signals of Co 2p3/2 and Co 2p1/2 were observed at the binding energy range of 775–810 eV. The Co 2p3/2 spectrum was deconvoluted into two peaks at 778.1 and 780.1 eV, which can be assigned to the binding energies of Co–S bonding. The Co^{2+}/Co^{3+} ratio is around 1:2, which coincides well with that in Co_3S_4 in the Co_3S_4/CNTs/C nanocomposites. Different from XRD (Figure 1a), no signals of the Co crystal phase were detected by XPS, indicating that the surface layer of Co_3S_4/CNTs/C is sulfurated by L-cysteine completely. Note that the small nanoparticles (~11 nm) located on the top of CNTs can be penetrated by XPS. This evidence suggests that the nanoparticles located on the top of CNTs are Co_3S_4 nanoparticles. The S 2p peaks in Figure 3c consist of the sulfur (S) 2p3/2 peak (161.5 eV) and the S 2p1/2 peak (162.1 eV), which confirmed the Co–S bonding. Besides Co and S elements, nitrogen (N) and C were also detected by XPS, and the N 1s spectrum was deconvoluted into pyrrolic nitrogen, graphitic nitrogen, and pyridinic nitrogen (Figure 3d). Carbon includes graphite-like carbon, graphite carbon, and C–N bonding carbon (Figure 3e), which was also confirmed by the Raman spectrum (Figure 3f) for the Co_3S_4/CNTs/C nanocomposites. As seen from Figure 3f, the D-band associated with disorders or defects (1350 cm^{-1}) and the G-band associated with highly ordered graphite (1580 cm^{-1}) were observed at a ratio of the intensity I_D/I_G = 1.09, where the D-band corresponds to sp^3-bonded carbon atoms and the G-band corresponds to sp^2-bonded carbon atoms. A D + D′ peak at 2930 cm^{-1} was also observed. Generally, the D + D′ band is a specific signal associated with defect density so that Figure 3f shows that the graphite carbon in the MOF-derived Co_3S_4/CNTs/C nanocomposites has a high defect density. In addition, the functional group of graphite carbon was also confirmed by FT-IR, as shown by the signal at 1620 cm^{-1} in Figure 3g. The surface area and porosity of these Co_3S_4/CNTs/C nanocomposites were studied by using nitrogen adsorption–desorption isotherms (Figure 3h,i). The Co_3S_4/CNTs/C nanocomposites exhibit a specific surface area of 62.74 cm^2 g^{-1}, a total pore volume of 0.17 cm^3 g^{-1}, and an average pore diameter of 10 nm, suggesting that the Co_3S_4/CNTs/C nanocomposites have a mesoporous structure.

2.2. Formation Mechanism. To clarify the formation mechanism, the ZIF-67 precursor was carbonized at 600 °C, and no dicyandiamide was used in the synthesis (Figure 4a). Co/C nanocomposites were obtained via this conventional pyrolysis process. Figure 4b reports the XRD pattern of the Co/C nanocomposites with the Co crystal phase (JCPDS no. 15-0806; cubic structure; space group: *Fm*-3*m* (225); a = 3.545 Å; vol = 44.5 $Å^3$). The peaks at 44.3°, 51.4°, and 75.8° correspond to the (111), (200), and (220) planes, respectively. The size of the Co nanoparticles was calculated based on the half-width of (111) and (200) diffraction peaks, and the values are 11.1 and 11.6 nm, respectively. The structure of the Co/C nanocomposites was also characterized by TEM, EDP, and high-resolution images (Figure 4c,d). Co nanoparticles dispersed in the carbon matrix have a diameter of about 10 nm. Figure 4e shows a high-resolution image of a Co/C nanocomposite, showing the monocrystal structure of the Co nanoparticle and the C-matrix around it. Based on the aforementioned results, Co nanoparticles acting as a catalyst for the growth of CNTs were generated in situ in the carbonization of the ZIF-67 precursor. The monodispersed characterization of Co nanoparticles led to monodispersed CNTs, and the diameter of the CNTs also depended on the

https://doi.org/10.1021/acsomega.1c05081
ACS Omega 2021, 6, 33855–33863

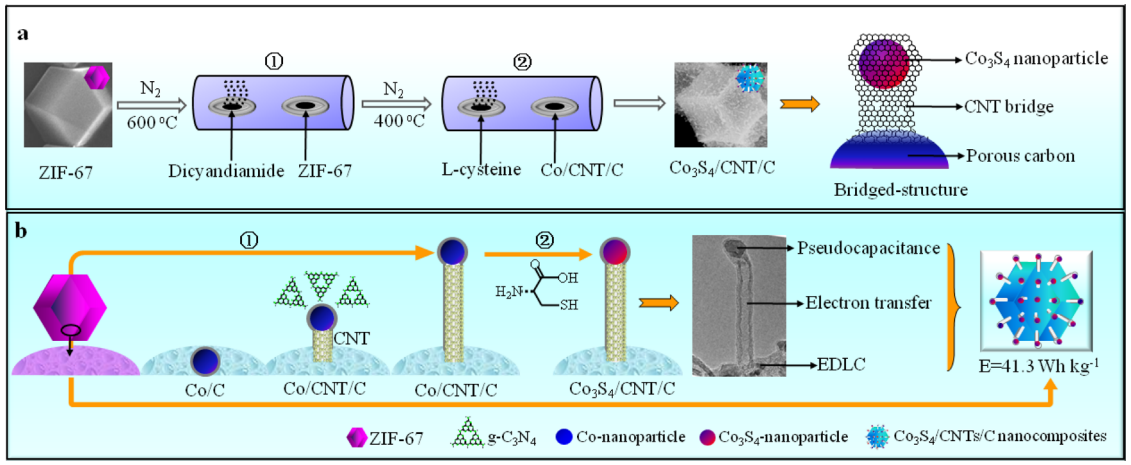

Figure 5. Schematic of the mechanism for the fabrication of Co_3S_4/CNTs/C nanocomposites as electrode materials with a combination function of EDLCs and pseudocapacitors. (a) Fabrication process of ZIF-67-derived Co_3S_4/CNTs/C nanocomposites; (b) growth and formation mechanisms of Co_3S_4/CNTs/C nanocomposites following the top-growth mechanism.

size of the Co nanoparticles, indicating a size-confinement effect.

Figure 5a illustrates the schematic process of synthesizing the MOF-derived Co_3S_4/CNTs/C nanocomposites, where Co nanoparticles generated in the dicyandiamide condition act as a catalyst first in preparing CNTs and serve as the source for the formation of Co_3S_4 nanoparticles at the end of the process. Co/CNTs/C composites were obtained first by a one-step carbonization of the ZIF-67 precursor, and Co_3S_4/CNTs/C nanocomposites were obtained by sulfuration with L-cysteine as the vulcanizing agent. The growth and formation mechanisms of the Co_3S_4/CNTs/C nanocomposites can be described as follows (Figure 5b). (1) ZIF-67 was obtained by using the method reported by our previous paper.[23] (2) The ZIF-67 precursor was then carbonized at 600 °C, and Co nanoparticles were obtained synchronously. Meanwhile, as the source of CNTs, a g-C_3N_4 atmosphere was produced by the pyrolytic elimination of dicyandiamide. (3) The Co nanoparticles captured g-C_3N_4 to produce CNTs, and the nanoparticles themselves were staying on the endmost of CNTs in the process. The CNTs grew from the inside to the surface of the porous carbon matrix and extended to the outside space. Following the top-growth mechanism, Co nanoparticles migrated along with the growth of CNTs. Monodispersed CNTs without entangling were then formed due to the monodispersion of Co nanoparticles. (4) Co_3S_4 nanoparticles were produced by sulfuration with L-cysteine as the vulcanizing agent at 400 °C, and they anchored on the topmost of CNTs. It is noteworthy that the Co nanoparticles in the porous carbon migrated from the inside to the outside and redistributed in the in situ growth of CNTs, which facilitated the sulfuration of Co to Co_3S_4.

We note that the residual Co phase is observed from the XRD patterns and the EDP of Co_3S_4/CNTs/C. To evaluate the efficiency of sulfuration, the characteristics of Co/C and Co_3S_4/CNTs/C were studied by hysteresis loop analysis (Figure 6). Both samples are ferromagnetic. The saturation magnetization, remanent magnetization, and coercivity of Co/C are 21.6 emu/g, 2.70 emu/g, and 111 Oe, respectively. The saturation magnetization, remanent magnetization, and coercivity of Co_3S_4/CNTs/C are 3.92 emu/g, 0.33 emu/g, and 80 Oe, respectively. Note that the Co/C and Co_3S_4/CNTs/C samples contain approximately 23.5 wt % Co. The normalized

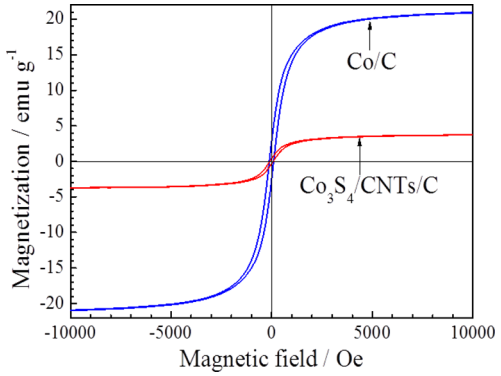

Figure 6. Hysteresis loops for the Co/C and Co_3S_4/CNTs/C nanocomposites measured at room temperature.

saturation magnetization values of Co/C and Co_3S_4/CNTs/C by the content of Co are 91.8 and 16.7 emu/g, respectively. The saturation magnetization of Co_3S_4/CNTs/C is significantly smaller than that of Co/C. This is understandable since most Co atoms (~82%) combined with S atoms to form a Co_3S_4 compound in Co_3S_4/CNTs/C. Note that the saturation magnetization of Co is greatly affected by the particle size. The saturation magnetization of the bulk Co crystal is 161 emu/g,[24] whereas the previously measured saturation magnetization values of Co nanoparticles with average particle sizes of ~15 and 27 nm are 79 and 158 ± 7 emu/g,[25] respectively. The decreased magnetization can be explained with the model of the spin-canted surface layer.[26] Briefly, the fine Co particles consist of two parts, a surface layer and an inner part. The magnetic moment of the surface layer cannot be turned entirely along the direction of the applied field, but it makes an average canting angle with the field, whereas the magnetic moment of the inner part can be aligned along the direction of the applied field. As a result, the saturation magnetization of the Co nanoparticles decreases with the decrease in particle size since the finer particles have a higher area of surface layer. The saturation magnetization of Co nanoparticles with an average particle size of ~20 nm in Co/C is only 91.8 emu/g, which is approximately 57% of the saturation magnetization of the bulk Co crystal. These data suggest that the saturation magnetization measured for Co/C should be reliable. In

https://doi.org/10.1021/acsomega.1c05081
ACS Omega 2021, 6, 33855−33863

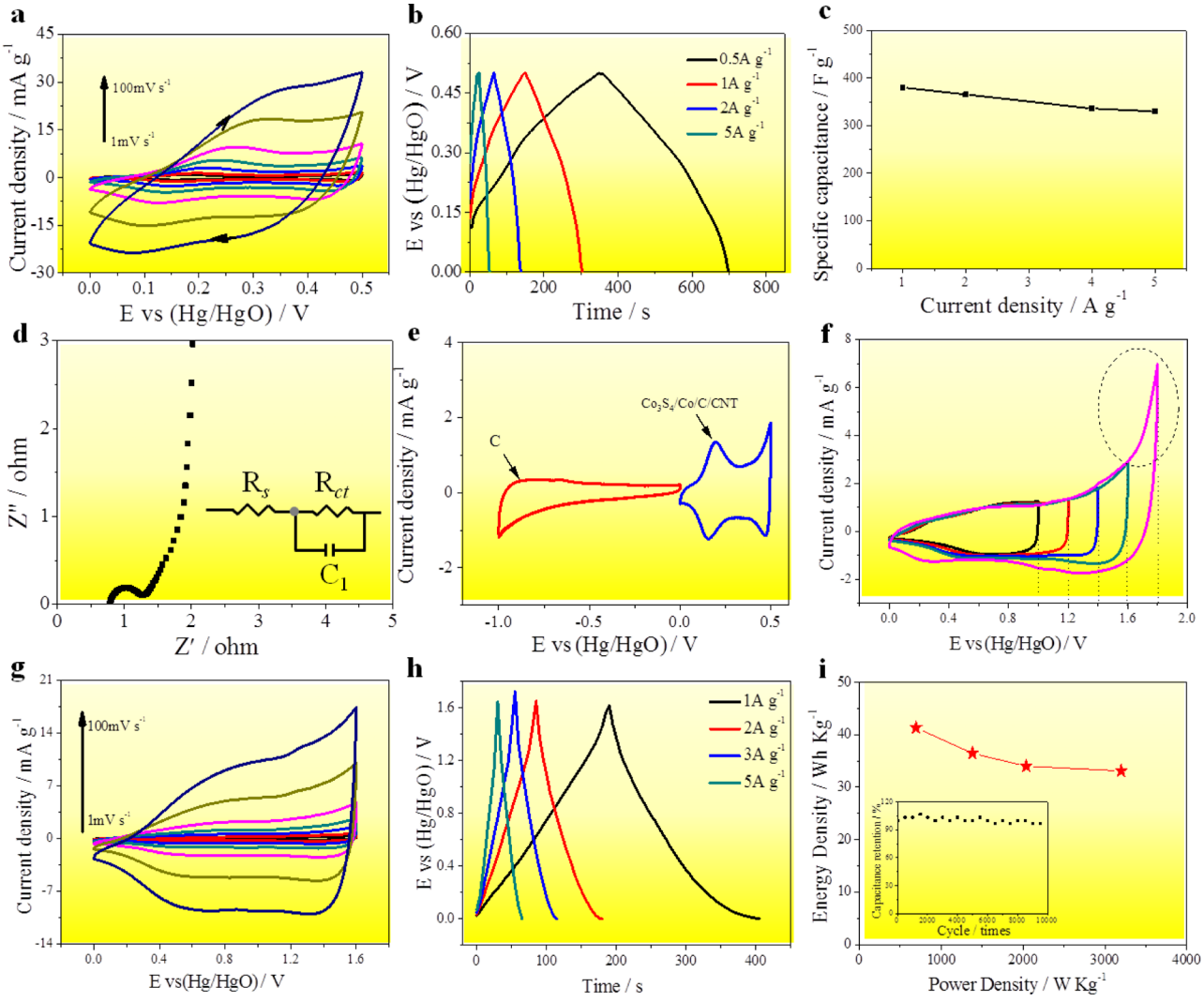

Figure 7. Electrochemical performance of the Co_3S_4/CNTs/C nanocomposite electrode: (a) cyclic voltammetry curves, (b) galvanostatic charge–discharge curves, (c) HRD, and (d) EIS. Electrochemical performance of the assembled asymmetric supercapacitor: (e) CV curves of the Co_3S_4/CNTs/C nanocomposites and activated carbon, (f) CV curves in different potential ranges, (g) CV curves in different scan rates, and (h) galvanostatic charge–discharge curves at different current densities. (i) Ragone plots of the assembled asymmetric supercapacitor (inset: cycling stability of the assembled asymmetric supercapacitor).

addition, the Co_3S_4 phase is paramagnetic and has a low susceptibility (in an order of 4×10^{-6}).[27] Based on the aforementioned results, saturation magnetization can be used to evaluate the residual Co content in Co_3S_4/CNTs/C nanocomposites.

2.3. Electrochemical Properties. The electrochemical performance of the MOF-derived Co_3S_4/CNTs/C nanocomposites as electrode materials was measured in 3 mol L^{-1} KOH. Figure 7a shows the cyclic voltammetry (CV) curves of the Co_3S_4/CNTs/C electrode materials at different scan rates (from 1 to 100 mV s^{-1}) with a potential range of 0.0 to 0.5 V. The near-rectangular shape of the CV curves revealed that the Co_3S_4/CNTs/C nanocomposites fabricated displayed a linear dependence of the charge on the charging potential. The charges were stored in the Co_3S_4 pseudocapacitive electrode through surface faradic redox reactions, rather than through the simple accumulation of ions on the surface. The calculated capacitances of the Co_3S_4/CNTs/C electrode materials are 524, 389, 363, 336, 303, 237, and 117 F g^{-1} at 1, 2, 5, 10, 20, 50, and 100 mV s^{-1}, respectively. Figure 7b gives the galvanostatic charge–discharge (GCD) curves of the Co_3S_4/CNTs/C electrode materials at current densities from 0.5 to 5 A g^{-1}. It can be clearly seen that the MOF-derived Co_3S_4/CNTs/C nanocomposites have a typical capacitance behavior with a nearly linear dependence of the stored charge on the width of the potential window, which coincides well with that of the CV curve. The Co_3S_4/CNTs/C nanocomposites presented a high specific capacitance of 380 F g^{-1} at a current density of 0.5 A g^{-1}, which remained at 330 F g^{-1} when the discharge current density was increased by five times (5 A g^{-1}), indicating a good high-rate discharge ability (Figure 7c). The specific capacitance of MOF-derived Co/C nanoparticles at a current density of 0.5 A g^{-1} was 146 F g^{-1},[23] which was about 38% of the specific capacitance (380 F g^{-1}) of Co_3S_4/CNTs/C nanocomposites. Based on these studies, the capacity contributions of the EDLCs (carbon materials) and pseudocapacitors (Co_3S_4) might be 38 and 62%, respectively.

Figure 7d shows the electrochemical impedance spectroscopy (EIS) of the Co_3S_4/CNTs/C electrode materials. An equivalent circuit was used (see the inset in Figure 7d), where

https://doi.org/10.1021/acsomega.1c05081
ACS Omega 2021, 6, 33855−33863

R_s, R_{ct}, and C_1 represent the internal resistance, the charge-transfer resistance of the electrochemical reaction, and the constant phase element in the EIS, respectively. The semicircle at the high-frequency region reflects the impedance of the electrochemical reaction. The impedance spectra were fitted with an equivalent circuit model (inset in Figure 7d) by using the least-square method with ZVIEW electrochemical impedance software. The fitted results show that the R_{ct} is about ~0.21 Ω for the Co_3S_4/CNTs/C nanocomposites.

An asymmetric Co_3S_4/CNTs/C||AC supercapacitor was assembled to further evaluate the Co_3S_4/CNTs/C electrode materials, where the Co_3S_4/CNTs/C nanocomposites and activated carbon were used as the positive and negative electrode materials (Figure 7e), respectively. The CV curves shown in Figure 7f were obtained in different potential windows at a scan rate of 10 mV s^{-1}, indicating that the optimal operating voltage is 1.6 V for the asymmetric supercapacitor. Figure 7g shows the CV curves of the asymmetric supercapacitor at various current densities in the potential range of 0−1.6 V. The specific capacitance calculated from CV of the asymmetric supercapacitor is 130 at 1 mV s^{-1}. The asymmetric supercapacitor presented a high specific capacitance of 105 F g^{-1} at a scan rate of 1 mV s^{-1}, which still remained at 79 F g^{-1} when the scan rate was increased to 100 mV s^{-1}. Figure 7h shows the GCD curves of the asymmetric supercapacitor at various current densities in the potential range of 0−1.6 V. Both the symmetrical shape of CV curves and the linear dependence of the GCD indicate a typical capacitance behavior as well as good reversibility. The energy density (Wh kg^{-1}) and power density (W kg^{-1}) of the Co_3S_4/CNTs/C nanocomposite electrode were evaluated by this constructed symmetrical supercapacitor. The Ragone plots of the asymmetric supercapacitor (Figure 7i) indicate that the specific energy density is 41.3 Wh kg^{-1} at a power density of 691.9 W kg^{-1}, with a higher maintenance of the energy density of 33.1 Wh kg^{-1} at a high power density of 3199.9 W kg^{-1}. In addition, the asymmetric supercapacitor exhibited high cycle stability with 100% capacitance retention after 10,000 cycles at 2 A g^{-1} (inset in Figure 7i), showing potentially wide applications.[28−32]

3. CONCLUSIONS

In this work, MOF-derived Co_3S_4/CNTs/C nanocomposites with a bridged structure were fabricated for the application in supercapacitors with a high energy density. As a catalyst for the formation of CNTs, Co nanoparticles were generated synchronously in the carbonization of the ZIF-67 precursor, and the monodispersed characterization of Co nanoparticles led to monodispersed CNTs without entangling. With the growth of CNTs, Co nanoparticles located on the endmost of CNTs migrated from the bulk of carbon to the surface, and Co/CNT/C nanocomposites were then produced. Sulfuration was used to convert Co nanoparticles to Co_3S_4 nanoparticles. As a result, the bridged structure can greatly maximize the efficiency of the Co_3S_4 nanoparticles acting as active electrode materials for pseudocapacitors and endow the Co_3S_4/CNTs/C nanocomposites with a high energy density, indicating that the bridged structure may be appropriate to combine the two electrode materials with different charge-storage mechanisms.

4. EXPERIMENTAL SECTION

4.1. Synthesis of Co_3S_4/CNTs/C Nanocomposites. Co_3S_4/CNTs/C nanocomposites were prepared with the following procedures: (1) $Co(NO_3)_2{\cdot}6H_2O$ (1.1641 g) was dissolved into 25 mL of methanol in a beaker, and 1.3136 g of 2-methylimidazole was dissolved into 25 mL of methanol in another beaker. (2) The two solutions were combined, the mixture was stirred for 10 min, and then the beaker was set for 24 h at 25 °C. (3) The mixture was centrifuged and dried in a vacuum oven at 60 °C for 12 h to obtain the ZIF-67 precursor. (4) Dicyandiamide (1.0 g) and the ZIF-67 precursor (0.1 g) were added in two quartz boats, respectively, and they were placed in a tube furnace. (5) The quartz boat was heated in a N_2 atmosphere to 600 °C at a heating rate of 2 °C min^{-1}, and the temperature was maintained for 1 h to obtain ZIF-67-derived Co/CNTs/C. Nitrogen as a carrier gas was injected into the tube furnace from the end close to the quartz boat containing dicyandiamide. (6) Similar to the last procedure, 1.2712 g of L-cysteine and 0.04 g of Co/CNTs/C nanocomposites were added in two quartz boats separately, they were put in the tube furnace, and L-cysteine was positioned at the upstream of the carrier gas. (7) The quartz boat was heated in the N_2 atmosphere at a heating rate of 2 °C min^{-1}, and the temperature was kept at 400 °C for 4 h to obtain MOF-derived Co_3S_4/CNTs/C nanocomposites.

4.2. Characterization. The crystal structure and morphology of the Co_3S_4/CNTs/C nanocomposite samples were determined with a Rigaku D/max 2500pc X-ray diffractometer operated at 40 kV (100 mA), an S-4800 scanning electron microscope at an acceleration voltage of 10 kV, and a JEM-2100 transmission electron microscope at 200 kV. Magnetic properties were measured at room temperature by using a LakeShore 7407 vibrating sample magnetometer with a maximum field of 20 kOe. XPS was performed on an ESCALAB 250Xi system. The Raman spectra were determined on a Renishaw Gloucestershire at a laser wavelength of 514 nm. Nitrogen adsorption−desorption isotherms were obtained using an ASAP-2020e system at 77 K, and Fourier transform infrared spectroscopy was carried out on a Bruker Vector 22 with a wavenumber ranging from 4000 to 400 cm^{-1}.

4.3. Electrochemical Characterization. Electrochemical measurements were performed in a standard three-electrode system composed of a Co_3S_4/CNTs/C electrode, a Pt electrode, and a HgO/Hg electrode. The working electrode was constructed by mixing the Co_3S_4/CNTs/C nanocomposites with a conductive agent (acetylene black) and binder (polyvinylidene fluoride) at a mass ratio of 80:10:10. The slurry was coated on a nickel cystosepiment and dried at 120 °C for 12 h under a vacuum. The working electrodes have a size of 1 cm × 1 cm, and their mass loading of active materials on the current collector is about 2 mg/cm^2. Electrochemical performances were tested on a BTS-5V 10 mA system with the voltage range of 0−0.5 V in 3 mol L^{-1} KOH electrolyte solution. Both of the CV tests and EIS were conducted on a CHI 660E electrochemical workstation. The asymmetrical supercapacitors were constructed by assembling an asymmetrical supercapacitor with Co_3S_4/CNTs/C nanocomposites as the positive electrode and homemade activated carbon as the negative electrode.

https://doi.org/10.1021/acsomega.1c05081
ACS Omega 2021, 6, 33855−33863

AUTHOR INFORMATION

Corresponding Authors

Yuqing Qiao − *Hebei Key Laboratory of Applied Chemistry, School of Environmental and Chemical Engineering and Clean Nano Energy Center, State Key Laboratory of Metastable Materials Science and Technology, Yanshan University, Qinhuangdao 066004, China*; Email: qiaoyq@ysu.edu.cn

Tifeng Jiao − *Hebei Key Laboratory of Applied Chemistry, School of Environmental and Chemical Engineering and Clean Nano Energy Center, State Key Laboratory of Metastable Materials Science and Technology, Yanshan University, Qinhuangdao 066004, China*; orcid.org/0000-0003-1238-0277; Email: tfjiao@ysu.edu.cn

Authors

Fan Wang − *Hebei Key Laboratory of Applied Chemistry, School of Environmental and Chemical Engineering, Yanshan University, Qinhuangdao 066004, China*

Na Li − *Hebei Key Laboratory of Applied Chemistry, School of Environmental and Chemical Engineering, Yanshan University, Qinhuangdao 066004, China*

Weimin Gao − *Hebei Key Laboratory of Applied Chemistry, School of Environmental and Chemical Engineering, Yanshan University, Qinhuangdao 066004, China*

Complete contact information is available at: https://pubs.acs.org/10.1021/acsomega.1c05081

Notes

The authors declare no competing financial interest.

ACKNOWLEDGMENTS

We greatly appreciate the financial supports of the National Natural Science Foundation of China (nos. 21872119 and 22072127) and the Natural Science Foundation of Hebei Province (no. B2020203037).

REFERENCES

(1) Wu, F.; Liu, M.; Li, Y.; Feng, X.; Zhang, K.; Bai, Y.; Wang, X.; Wu, C. High-Mass-Loading Electrodes for Advanced Secondary Batteries and Supercapacitors. *Electrochem. Energy Rev.* **2021**, *4*, 382−446.

(2) Forse, A. C.; Merlet, C.; Griffin, J. M.; Grey, C. P. New Perspectives on the Charging Mechanisms of Supercapacitors. *J. Am. Chem. Soc.* **2016**, *138*, 5731−5744.

(3) Wang, Y.; Song, Y.; Xia, Y. Electrochemical capacitors: mechanism, materials, systems, characterization and applications. *Chem. Soc. Rev.* **2016**, *45*, 5925−5950.

(4) Yan, S.; Abhilash, K. P.; Tang, L.; Yang, M.; Ma, Y.; Xia, Q.; Guo, Q.; Xia, H. Research Advances of Amorphous Metal Oxides in Electrochemical Energy Storage and Conversion. *Small* **2019**, *15*, 1804371.

(5) Jia, P.; Yang, T.; Liu, Q.; Yan, J.; Shen, T.; Zhang, L.; Liu, Y.; Zhao, X.; Gao, Z.; Wang, J.; Tang, Y.; Huang, J. In-situ imaging Co_3O_4 catalyzed oxygen reduction and evolution reactions in a solid state Na-O_2 battery. *Nano Energy* **2020**, *77*, 105289.

(6) Yang, T.; Li, H.; Chen, J.; Ye, H.; Yao, J.; Su, Y.; Guo, B.; Peng, Z.; Shen, T.; Tang, Y.; Zhang, L.; Huang, J. In situ imaging electrocatalytic CO_2 reduction and evolution reactions in all-solid-state Li-CO_2 nanobatteries. *Nanoscale* **2020**, *12*, 23967−23974.

(7) Zou, Y.; Zhang, W.; Chen, N.; Chen, S.; Xu, W.; Cai, R.; Brown, C. L.; Yang, D.; Yao, X. Generating Oxygen Vacancies in MnO Hexagonal Sheets for Ultralong Life Lithium Storage with High Capacity. *ACS Nano* **2019**, *13*, 2062−2071.

(8) Torad, N. L.; Salunkhe, R. R.; Li, Y.; Hamoudi, H.; Imura, M.; Sakka, Y.; Hu, C. C.; Yamauchi, Y. Electric Double-Layer Capacitors Based on Highly Graphitized Nanoporous Carbons Derived from ZIF-67. *Chem. − Eur. J.* **2014**, *20*, 7895−7900.

(9) Salunkhe, R. R.; Tang, J.; Kobayashi, N.; Kim, J.; Ide, Y.; Tominaka, S.; Kim, J. H.; Yamauchi, Y. Ultrahigh performance supercapacitors utilizing core−shell nanoarchitectures from a metal-organic framework-derived nanoporous carbon and a conducting polymer. *Chem. Sci.* **2016**, *7*, 5704−5713.

(10) Hou, L.; Du, Q.; Su, L.; Di, S.; Ma, Z.; Chen, L.; Shao, G. Ni-Co layered double hydroxide with self-assembled urchin like morphology for asymmetric supercapacitors. *Mater. Lett.* **2019**, *237*, 262−265.

(11) Song, A.; Cao, L.; Yang, W.; Yang, W.; Wang, L.; Ma, Z.; Shao, G. In situ construction of nitrogen-doped graphene with surface-grown carbon nanotubes as a multifactorial synergistic catalyst for oxygen reduction. *Carbon* **2019**, *142*, 40−50.

(12) Mohammadi, A.; Arsalani, N.; Tabrizi, A. G.; Moosavifard, S. E.; Naqshbandi, Z.; Ghadimi, L. S. Engineering rGO-CNT wrapped Co_3S_4 nanocomposites for high-performance asymmetric supercapacitors. *Chem. Eng. J.* **2018**, *334*, 66−80.

(13) Chaikittisilp, W.; Hu, M.; Wang, H.; Huang, H.-S.; Fujita, T.; Wu, K. C.-W.; Chen, L.-C.; Yamauchi, Y.; Ariga, K. Nanoporous carbons through direct carbonization of a zeolitic imidazolate framework for supercapacitor electrodes. *Chem. Commun.* **2012**, *48*, 7259−7261.

(14) Ko, Y.; Shin, M. D.; Koo, B.; Lee, S. W.; Yoon, W. S.; Cho, J. H. Ultrathin supercapacitor electrodes with high volumetric capacitance and stability using direct covalent-bonding between pseudocapacitive nanoparticles and conducting materials. *Nano Energy* **2015**, *12*, 612−625.

(15) Sikdar, N.; Konkena, B.; Masa, J.; Schuhmann, W.; Maji, T. K. Co_3O_4@Co/NCNT Nanostructure Derived from a Dicyanamide-Based Metal-Organic Framework as an Efficient Bi-functional Electrocatalyst for Oxygen Reduction and Evolution Reactions. *Chem. − Eur. J.* **2017**, *23*, 18049−18056.

(16) Jiang, Z.; Lu, W.; Li, Z.; Ho, K.; Li, X.; Jiao, X.; Chen, R. Synthesis of amorphous cobalt sulfide polyhedral nanocages for high performance supercapacitors. *J. Mater. Chem. A* **2014**, *2*, 8603−8606.

(17) Li, Y.; Wang, G.; Wei, T.; Fan, Z.; Yan, P. Nitrogen and sulfur co-doped porous carbon nanosheets derived from willow catkin for supercapacitors. *Nano Energy* **2016**, *19*, 165−175.

(18) Salunkhe, R. R.; Tang, J.; Kamachi, Y.; Nakato, T.; Kim, J. H.; Yamauchi, Y. Asymmetric Supercapacitors Using 3D Nanoporous Carbon and Cobalt Oxide Electrodes Synthesized from a Single Metal−Organic Framework. *ACS Nano* **2015**, *9*, 6288−6296.

(19) Yang, J.; Zeng, C.; Wei, F.; Jiang, J.; Chen, K.; Lu, S. Cobalt-carbon derived from zeolitic imidazolate framework on Ni foam as high-performance supercapacitor electrode material. *Mater. Des.* **2015**, *83*, 552−556.

(20) Wang, Q.; Jiao, L.; Du, H.; Si, Y.; Wang, Y.; Yuan, H. Co_3S_4 hollow nanospheres grown on graphene as advanced electrode materials for supercapacitors. *J. Mater. Chem. A* **2012**, *22*, 21387−21391.

(21) Yan, Y.; Li, K.; Chen, X.; Yang, Y.; Lee, J.-M. Heterojunction-Assisted Co_3S_4@Co_3O_4 Core-Shell Octahedrons for Supercapacitors and Both Oxygen and Carbon Dioxide Reduction Reactions. *Small* **2017**, *13*, 1701724.

(22) Zhang, X.; Chen, A.; Zhong, M.; Zhang, Z.; Zhang, X.; Zhou, Z.; Bu, X.-H. Metal-Organic frameworks (MOFs) and MOF-derived materials for energy storage and conversion. *Electrochem. Energy Rev.* **2019**, *2*, 29−104.

(23) Li, X.; Qiao, Y.; Wang, C.; Shen, T.; Zhang, X.; Wang, H.; Li, Y.; Gao, W. MOF-derived Co/C nanocomposites encapsulated by $Ni(OH)_2$ ultrathin nanosheets shell for high performance supercapacitors. *J. Alloys Compd.* **2019**, *770*, 803−812.

(24) Shao, H.; Huang, Y.; Lee, H.; Suh, Y.; Kim, C. Cobalt nanoparticles synthesis from $Co(CH_3COO)_2$ by thermal decomposition. *J. Magn. Magn. Mater.* **2006**, *304*, e28−e30.

(25) El-Gendy, A. A.; Ibrahim, E. M. M.; Khavrus, V. O.; Krupskaya, Y.; Hampel, S.; Leonhardt, A.; Büchner, B.; Klingeler, R. The synthesis of carbon coated Fe, Co and Ni nanoparticles and an examination of their magnetic properties. *Carbon* **2009**, *47*, 2821−2828.
(26) Han, D. H.; Wang, J. P.; Luo, H. L. Crystallite size effect on saturation magnetization of fine ferrimagnetic particles. *J. Magn. Magn. Mater.* **1994**, *136*, 176−182.
(27) Heidelberg, R. F.; Luxem, A. H.; Talhouk, S.; Banewicz, J. J. The Magnetic Susceptibilities of the Cobalt-Sulfur System. *Inorg. Chem.* **1966**, *5*, 194−197.
(28) Xu, Y.; Wang, R.; Wang, J.; Li, J.; Jiao, T.; Liu, Z. Facile fabrication of molybdenum compounds (Mo_2C, MoP and MoS_2) nanoclusters supported on N-doped reduced graphene oxide for highly efficient hydrogen evolution reaction over broad pH range. *Chem. Eng. J.* **2021**, *417*, 129233.
(29) Geng, R.; Chang, R.; Zou, Q.; Shen, G.; Jiao, T.; Yan, X. Biomimetic Nanozymes Based on Coassembly of Amino Acid and Hemin for Catalytic Oxidation and Sensing of Biomolecules. *Small* **2021**, *17*, 2008114.
(30) Bai, J.; Wang, R.; Ju, M.; Zhou, J.; Zhang, L.; Jiao, T. Facile preparation and high performance of wearable strain sensors based on ionically cross-linked composite hydrogels. *Sci. China Mater.* **2021**, *64*, 942−952.
(31) Wang, R.; Yan, X.; Ge, B.; Zhou, J.; Wang, M.; Zhang, L.; Jiao, T. Facile Preparation of Self-Assembled Black Phosphorus-Dye Composite Films for Chemical Gas Sensors and Surface-Enhanced Raman Scattering Performances. *ACS Sustainable Chem. Eng.* **2020**, *8*, 4521−4536.
(32) Yin, J.; Zhan, F.; Jiao, T.; Wang, W.; Zhang, G.; Jiao, J.; Jiang, G.; Zhang, Q.; Gu, J.; Peng, Q. Facile preparation of self-assembled MXene@Au@CdS nanocomposite with enhanced photocatalytic hydrogen production activity. *Sci. China Mater.* **2020**, *63*, 2228−2238.

https://doi.org/10.1021/acsomega.1c05081
ACS Omega 2021, 6, 33855−33863